Chinese Chemical Letters 33 (2022) 1058–1064

Contents lists available at ScienceDirect

Chinese Chemical Letters

journal homepage: www.elsevier.com/locate/cclet

A comparative study on the reactivity of cationic niobium clusters with nitrogen and oxygen

Benben Huang[a,b], Mengzhou Yang[a,b], Xin Lei[b], Wen Gan[a,b], Zhixun Luo[a,*]

[a] *Beijing National Laboratory for Molecular Sciences (BNLMS), State Key Laboratory for Structural Chemistry of Unstable and Stable Species, Institute of Chemistry, Chinese Academy of Sciences, Beijing 100190, China*
[b] *University of Chinese Academy of Sciences, Beijing 100049, China*

ARTICLE INFO

Article history:
Received 22 February 2021
Revised 1 April 2021
Accepted 12 April 2021
Available online 19 April 2021

Keywords:
Gas phase reaction
Nb cluster
Chemical adsorption
Orbital analysis
Energy decomposition analysis

ABSTRACT

We have prepared well-resolved Nb_n^+ (n = 1–10) clusters and report here an in-depth study on the essentially different reactivity with N_2 and O_2, by utilizing a multiple-ion laminar flow tube reactor in tandem with a customized triple quadrupole mass spectrometer (MIFT-TQMS). As results, the Nb_n^+ clusters are found to readily react with N_2 and form adsorption products $Nb_nN_{2m}^+$; in contrast, the reactions with O_2 give rise to $Nb_nO_{1-4}^+$products, and the odd-oxygen products indicate O-O bond dissociation, as well as increased mass abundance of NbO^+ pertaining to oxygen-etching reactions. We illustrate how N_2 prefers a physical adsorption on Nb_n^+clusters with an end-on orientation for all the products, and allow for size-selective Nb_n^+clusters to act as electron donor or acceptor in forming $Nb_nN_{2m}^+$. In contrast to these nitrides, the dioxides $Nb_nO_2^+$display much larger binding energies, with O_2 always as an electron acceptor, corresponding to superoxide or peroxide states in the initial reactions. Density-of-states and orbital analyses show that the interactions between Nb_n^+ and O_2 are dominated by strong π-backdonation indicative of incidental electron transfer; whereas weak π-backdonation and simultaneous σ donation interactions exist in $Nb_nN_2^+$. Further, reaction dynamics analysis illustrates the different interactions for N_2 and O_2 in approaching the Nb_n^+ clusters, showing the energy diagrams for N_2 adsorption and O-O bond dissociation in producing odd-oxygen products. Fragment analyses with orbital correlation and donor-acceptor charge transfer are also performed, giving rise to full insights into the reactivities and interactions of such transition metal clusters with typical diatomic molecules.

Gas adsorption is one of the most basic interfacial phenomena and closely related to diverse applications in industrial and agricultural production and daily life. People may take it for granted that the adsorption of gas molecules on the metals is simply divided into physical adsorption and chemical adsorption; however, the underlying mechanism that determines the diverse interactions and surface reactivity at reduced sizes are illusive to be fully understood. The study of gas adsorption on solid surfaces is helpful to understand the micro-mechanism of various physicochemical processes; also, adsorption of gas molecules on nanometals is a key step in catalytic processes and important for various gas phase reactions. While physisorption is often dominated by molecular van-der Waals force and generally emits rare energies, chemisorption can be largely exothermic and may involve covalent interactions and stepwise reactions [1]. In this regard, molecular adsorption can be associated with three processes, *i.e.*, inactivated adsorption, activated adsorption and precursor-mediated adsorptions [2]. The adsorbate may reach a chemisorption state through a barrierless process directly from physisorption state; or it needs to overcome a potential barrier simply by heating or other reaction conditions; or undergoes a precursor-mediated adsorption, where the chemisorbed state could be attained through a precursor intermediate.

On this basis, the reactivities of transition metal clusters with small molecules have been extensively studied, illustrating the distinction of physical and chemical adsorptions on surfaces [2]. Also, the interaction mechanisms and properties of metal cluster complexes have been widely analyzed by joint experimental and theoretical studies. Among them, niobium clusters have been an important research object unveiling size-dependent chemical and physical properties of transition metals at reduced sizes [3–10]. Combining mass spectrometry and gas flow reactors [11,12], the reac-

---

[*] Corresponding author.
E-mail address: zxluo@iccas.ac.cn (Z. Luo).

https://doi.org/10.1016/j.cclet.2021.04.020

tivities of niobium clusters with many chemicals have been studied, such as H_2 [12–15], O_2 [16,17], N_2 [18,19], CO_x [20–22], NO_x [23,24] and hydrocarbons [25–29]. The reactions of Nb clusters with N_2 and H_2 ($/D_2$) have similar adsorptive patterns; while the reaction with O_2 shows a difference due to the differences of atomic valence configuration and bonding nature of these diatomic molecules. In general, N_2 is inert in most reactions due to a very high dissociation energy (945 kcal/mol) of the N≡N triple bond and a high HOMO-LUMO gap (~10.82 eV); in comparison, ground-state O_2 is in triplet with two spin single electrons pertaining to its high activity [30]. However, it is not fully unveiled how the stability of such metal clusters and atomic valence configuration and bonding nature cooperatively determine the experimental observation on their reactivity.

On the other hand, previously published studies have also estimated the reaction rate constants for niobium clusters with N_2 and O_2 showing a likely difference of three orders of magnitude [18,19]. Further studies reported the similar adsorption of N_2 on niobium clusters [18,19,31], and there are adsorption products of polynitrogen molecules depending on the pressure and concentration of the reaction gas at room temperature [32]. For example, Pillai *et al.* [33] generated $Nb^+(N_2)_n$ complexes (n = 3–16) with nitrogen as buffer gas and investigated the vibration in forming such complexes by infrared photodissociation spectroscopy (IRPD), showing a preferred coordination of six ligands. Meanwhile, the reactions of small Nb_n^+ (n = 1–3) with O_2 have been studied by Loh *et al.* [16] who measured the cross section as a function of kinetic energy and proposed dissociation pathways and threshold values. It is anticipated that these experimental cluster physics studies of such small Nb clusters can be connected with theorical energy calculations in determining the thermodynamics and their reaction dynamics in gas phase [34].

On these bases, here we have performed a further in-depth study of the thermalized gas-phase Nb_n^+ (n = 1–10) clusters in reacting with sufficient N_2 and O_2 gas in a customized multiple ions laminar flow tube in tandem with triple quadrupole mass spectrometer (MIFT-TQMS). It is found that the Nb_n^+ clusters, produced by the home-made magnetron sputtering (MagS) source, readily react with both N_2 and O_2, but form different series of products respectively, seen as $Nb_nN_{2m}^+$ (m = 1–3) and $Nb_nO_x^+$ (x = 1–4). Theoretical calculations results reveal that the $Nb_nN_{2m}^+$ clusters all adopt end-on orientation adsorption for N_2 on Nb_n^+ with much smaller binding energy than that of correlative $Nb_nO_2^+$ series which correspond to strong hollow-site adsorption allowing for occasional dissociative adsorption. Further, we conducted a comprehensive study thermodynamic energetics, HOMO-LUMO gaps, charge transfer, Wiberg bond index (WBI), density of state (DOS), natural atomic orbital (NAO) and energy decomposition analyses based on natural orbitals for chemical valence (EDA-NOCV). In addition, we carried out potential scan for N_2 and O_2 in approaching an Nb_n^+ cluster until the formation of $Nb_3N_2^+$ and $Nb_3O_2^+$, illustrating how cluster-molecule interactions initiate their reaction. Finally, we explore the reaction pathways of both N_2 and O_2 with Nb_3^+ as a representative, demonstrate the N_2-adsorption behavior and the reaction dynamics in producing $Nb_3O_2^+$ from O_2-adsorption, to dissociative intermediate, and to ultimately exhaust of NbO ($/NbO^+$).

The experiments in this study are conducted on our customized multi-ions laminar flow tube reactor in tandem with a triple quadrupole mass spectrometer (MIFT-TQMS). A self-designed MagS source with a DC power supply of 5 kW was used to obtain the clean mass distributions of small niobium clusters [35]. A niobium disk (99.95% purity, 50.8 mm diameter, 4 mm thickness) was used as the sputtering target. High-purity helium (>99.999%) and high-purity argon (>99.995%) were used as carrier gas and sputtering work gas, introduced from the rare of the MagS source and the magnetron head respectively, with the gas flow rates controlled by two mass flowmeters (Alicat, a range of 0–100 sccm and 0–100 slm, respectively). Typical parameters for the MagS source to produce the niobium clusters with n = 1–10 are: 170 V DC voltage, 4 A current, a background pressure of source chamber at ~7 Torr, He carrier gas at ~12 slm helium, while Argon is 60–120 sccm. Different concentrations of N_2 and O_2 (*ca.*, 0.5%–30% in He) are injected into the flow tube (60 mm diameter, 1 m long) which is maintained at 0.9 Torr pressure for stable laminar flow and sufficient collisional reaction. The detailed values for these parameters may differ with dependence on the target situation and vacuum status, *etc.*

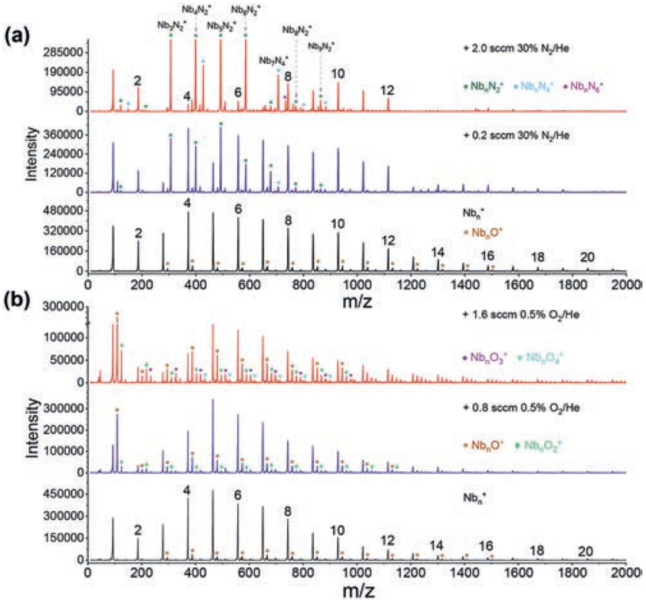

Fig. 1. The mass spectra of Nb_n^+ clusters in the absence and presence of (a) 30% N_2/He and (b) 0.5% O_2/He, respectively. The weak mass peaks marked with stars (*) in the nascent Nb_n^+cluster distributions correspond to trace amount of oxygen contamination.

All the DFT calculations were performed using Gaussian 09 software package [36]. B3LYP exchange-correlation functional was used to optimize the geometric structures of all the niobium clusters and products, the basis sets of Lanl2dz was used for Nb with an extra *d* polarization function, while 6–311G(d) for N and O atoms [36,37]. Vibrational frequency calculations were performed for each of the optimized structures and zero-point vibrations were corrected for all the energy calculations. Thermodynamic data, Wiberg bond index (WBI), partial density of states (PDOS), natural atomic orbital (NAO) and electron configuration are analyzed by using the Multiwfn software [38]. The geometric structures, frontier orbitals, charge distributions by natural population analysis (NPA), and the PDOS patterns of the Nb_n^+, $Nb_nN_2^+$, $Nb_nO_2^+$ (n = 1–10) are plotted by visual molecular dynamics (VMD) [39]. Energy decomposition analysis was conducted based on natural orbitals for chemical valence (EDA-NOCV), calculated with Amsterdam Density Functional (ADF) program [40,41] at the B3LYP/TZP level of theory.

Fig. 1 presents the mass spectra of the Nb_n^+ (n = 1–21) clusters in the absence and presence of N_2 and O_2 gas reactants respectively, where the concentrations and gas flowrates are controlled by a mass flowmeter (ALICAT-LD12). As is shown in Fig. 1a, most of the Nb_n^+ clusters react with N_2 just to form molecular adsorption products $Nb_nN_{2m}^+$ (m = 1–3) with size dependence, which is in contrast to the sequence reactions between Nb_n^+ and O_2 in forming $Nb_nO_x^+$ (x = 1–4). From mass spectra in Fig. 1a and the

Table 1

DFT-calculated energies (eV) for the likely diverse reaction pathways of Nb_n^+ (n = 1–10) with O_2. All the data are calculated at the B3LYP/Lanl2dz level for Nb_n^+ and B3LYP/6-311G(d) level for N/O.

Reaction channel	1	2	3	4	5	6	7	8	9	10
$Nb_n^+ + O_2 \rightarrow Nb_nO_2^+$	−2.28	−3.67	−3.60	−2.77	−3.15	−2.80	−3.05	−2.53	−2.93	−2.90
$Nb_n^+ + O_2 \rightarrow Nb_{n\text{-}1}O^+ + NbO$		−5.04	−3.99	−4.54	−4.65	−4.42	−3.99	−3.71	−4.14	−3.13
$Nb_n^+ + O_2 \rightarrow Nb_{n\text{-}1}O + NbO^+$		−5.04	−3.60	−2.00	−2.66	−2.31	−1.50	−1.25	−1.60	−1.08
$Nb_n^+ + O_2 \rightarrow Nb_{n-1}^+ + NbO_2$		−4.38	−3.35	−2.96	−3.72	−3.54	−2.94	−3.18	−3.68	−3.09
$Nb_n^+ + O_2 \rightarrow Nb_{n\text{-}1} + NbO_2^+$		−3.08	−1.83	−0.62	−1.04	−0.58	0.10	−0.11	−0.74	0.46
$Nb_n^+ + O_2 \rightarrow Nb_{n-2}^+ + 2NbO$			−1.03	0.39	0.02	−0.57	0.22	0.59	−0.15	−0.07
$Nb_n^+ + O_2 \rightarrow Nb_{n-2}^+ + Nb_2O_2$			3.58	5.00	4.62	4.04	4.83	5.19	4.45	4.54
$Nb_n^+ + O_2 \rightarrow Nb_{n\text{-}1}\ O_2 + Nb^+$		0.26	1.41	2.74	2.19	2.57	3.72	3.18	3.06	3.43
$Nb_n^+ + O_2 \rightarrow Nb_{n\text{-}1}\ O_2^+ + Nb$		1.04	0.68	1.14	1.21	1.01	1.97	1.48	1.49	1.68

variation of mass abundances of the nascent Nb_n^+ clusters and $Nb_nN_{2m}^+$ products (Fig. S1 in Supporting information), it is seen that Nb_{3-6}^+ clusters react faster than the other clusters and convert to $Nb_nN_2^+$ products. In comparison, the Nb_7^+ is seen to prefer an adsorption of several nitrogen molecules to form $Nb_7N_{4,6}^+$ (also seen for Nb_4^+); The cation Nb^+, also Nb_8^+ and Nb_9^+ slowly react with N_2, but Nb_2^+ and Nb_{10}^+ display rare reaction products with N_2 in the experimental condition of this study. The variation of Nb_n^+ clusters reacting with N_2 reflects their size-dependent stability and reactivity, assuming they undergo identical collision annihilation with the wall of the flow tube. We have plotted the changes in relative intensity of Nb_n^+ (n = 3–9) and $-\ln(I/I_0)$ of Nb_n^+ as a function of the gas flow rate (Fig. S3 in Supporting information). The experimental results display that the N_2 addition on Nb_n^+ (n = 1–10) closely follow the quasi first-order reactions for which the rate constants have been estimated simply by using the equation $\ln(I_A/I_0) = -k_1(P_e\Delta t/k_BT)$ [42], where k_B is the Boltzmann constant, T is the temperature, P_e and Δt correspond to the effective pressure and reaction time. As results, the size-dependent reaction rates of Nb_n^+ (n = 1–10) exhibit a wide diversity, and Nb_3^+ is found to display a maximal value of ~10^{-9} cm^3 $molecule^{-1}$ s^{-1}.

There is different case. As shown in Fig. 1b, the Nb_n^+ (n = 1–10) clusters are highly reactive with O_2 even at a very low concentration (*e.g.*, 0.8 sccm of 0.5% O_2 in He gas). Even in the presence of a small amount of oxygen, the dissociative products Nb_nO^+ are observed. This is reasonable considering the large Nb-O bond energy up to ~770 kJ/mol which is even larger than the O-O bond strength (~400 kJ/mol); and electron transfer readily occur between niobium and oxygen [43,44], with a variety of exothermic reaction channels as given in Table 1. Among the thermodynamically favorable channels, the O_2-dissociaed equation to produce a NbO neutral suggests the maximal energy release for all the Nb_n^+ (n = 2–10) clusters. This could well explain the experimental observation of dissociative products Nb_nO^+ which was also found in previous experimental study [17]. It is worth noting that, such a favorable reaction channel "$Nb_n^+ + O_2 \rightarrow Nb_{n\text{-}1}O^+ + NbO$" largely differs from the previously determined reactions of "$Al_n^+ + O_2 \rightarrow Al_m^+ + Al_{n\text{-}m}O_2$" [45], "$Al_n^- + O_2 \rightarrow Al_{n-4}^- + 2Al_2O$" [46] and "$Co_n^- + O_2 \rightarrow Co_{n-1}^- + CoO_1^-$" [47]. Due to the large Nb-O bond energy, here the reaction channels with $Nb^{0/+}$ or $Nb_2^{0/+}$ removal are much less favorable from the thermodynamics, which is well consistent with the experimental observation that Nb^+ and Nb_2^+ do not display increased mass abundance in the varied reaction conditions. Also, this is consistent with the previous study by Radi *et al.* [17], where the dominant reaction pathway of mass-selected small niobium clusters with O_2 in a drift reactor was proposed to be the one in producing primary products of NbO and NbO^+.

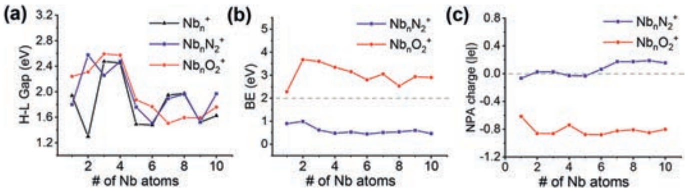

Fig. 2. (a) DFT-calculated HOMO-LUMO gaps of Nb_n^+, $Nb_nN_2^+$ and NbO_2^+ (n = 1–10). (b) Binding energy of $Nb_nN_2^+$ and $Nb_nO_2^+$. (c) NPA charge transfer of Nb_n^+ to N_2 in $Nb_nN_2^+$ compared with Nb_n^+ to O_2 in $Nb_nO_2^+$. All the data are calculated at the B3LYP/Lanl2dz level for Nb_n^+ and B3LYP/6-311G(d) level for N/O.

Utilizing DFT calculations we have provided further insights into the diverse reactivities of niobium clusters (for details of the lowest-energy structures, spin multiplicity, bond lengths, and point group see Fig. S6 in Supporting information). For the adsorption complexes, N_2 adopts an end-on adsorption orientation on the Nb_n^+ clusters of which the nascent structures and spin multiplicities almost do not change, except $Nb_2N_2^+$ which shows a *V*-shape structure with a high spin multiplicity. In contract, $Nb_nO_2^+$ (n > 2) clusters all adopt hollow-site adsorption mode with elongated O-O bond length ranging from 1.2 Å to 1.5 Å, although the structures of Nb_n^+ in $Nb_nO_2^+$ do not show much changes. Moreover, the spin multiplicities of the odd-number small niobium clusters (*i.e.*, $Nb_{2n+1}O_2^+$) reduced in the formation of $Nb_nO_2^+$ (except $Nb_9O_2^+$); whereas, for the even-number niobium clusters (*i.e.*, Nb_{2n}^+), the spin of the cluster can be aligned opposite to that of the $^3O_2$ molecule thus spin conservation in the $Nb_{2n}O_2^+$ products [48,49].

Fig. 2 plots the DFT-calculated HOMO-LUMO gaps, binding energies (BE), and natural population analysis (NPA) of charge distributions of the Nb_n^+, $Nb_nN_2^+$ and NbO_2^+ (n = 1–10) clusters. More energetics data such as the VSE, ASE, binding energy per atom (BE) and Δ_2E of the Nb_n^+ are given in Fig. S9 (Supporting information). While no surprise that the $Nb_nN_2^+$ clusters show much smaller cluster-molecule binding energies and charge transfer comparing with that of the $Nb_nO_2^+$ products, the HOMO-LUMO gaps of the nascent Nb_n^+ clusters and the subsequent $Nb_nN_2^+$ and $Nb_nO_2^+$ are comparable with each other except a jump at n = 2,7,8 pertaining to altered spin multiplicity ($Nb_7O_2^+$), symmetry ($Nb_2O_2^+$) or structure changes ($Nb_8O_2^+$). Note that, O_2 always serves as an electron acceptor in interacting with the Nb_n^+ clusters, with a total electron transfer of 0.6–0.9 |e|, which is in sharp contrast to that of the $Nb_nN_2^+$ complexes of which the σ donations from N≡N to the Nb_n^+ clusters are enabled especially for the larger ones at $n \geq 6$. Detailed information about NPA charge and natural electron configuration of $Nb_{3/6}^+$, N_2, O_2, $Nb_{3/6}N_2^+$ and $Nb_{3/6}O_2^+$ is shown in Tables S3 and S4 (Supporting information).

Table 2 lists the Wiberg bond indexes (WBI) between the atoms in $Nb_nN_2^+$ and $Nb_nO_2^+$ (n = 1–10). As is shown, every WBI of the N(1)-N(2) bond in $Nb_nN_2^+$ changes to 2.69-2.90 from the primary N≡N triple bond in dinitrogen. Meanwhile, the WBI of the linked N(1)-Nb bond is about 0.3–0.5, while the WBI of N(2)-Nb is as small as 0.05–0.15 indicating weak interaction between the Nb_n^+ clusters and N_2 corresponding to physical adsorption. By contrast,

Table 2
The WBI analysis between the atoms in $Nb_nN_2^+$ and $Nb_nO_2^+$ (n = 1–10).

Species		1	2	3	4	5	6	7	8	9	10
$Nb_nN_2^+$	N(1)-Nb	0.32	0.30	0.45	0.48	0.46	0.43	0.40	0.43	0.44	0.41
	N(2)-Nb	0.08	0.06	0.11	0.16	0.14	0.10	0.05	0.06	0.06	0.07
	N(1) -N(2)	2.80	2.88	2.81	2.72	2.69	2.81	2.92	2.90	2.89	2.90
$Nb_nO_2^+$	O(1)-Nb(1)	1.02	0.48	0.49	0.45	0.51	0.53	0.39	0.34	0.33	0.39
	O(2)-Nb(1)	1.02	0.48	0.49	0.45	0.38	0.35	0.34	0.39	0.33	0.39
	O(1)-Nb(2)		0.48	0.43	0.46	0.43	0.33	0.42	0.51	0.47	0.48
	O(2)-Nb(2)	–	0.48	–	–	–	–	–	–	–	–
	O(2)-Nb(3)	–	–	0.42	0.46	0.36	0.45	0.54	0.48	0.47	0.48
	O(1)-O(2)	1.04	1.02	1.02	1.00	1.00	0.95	1.00	0.98	1.00	0.98

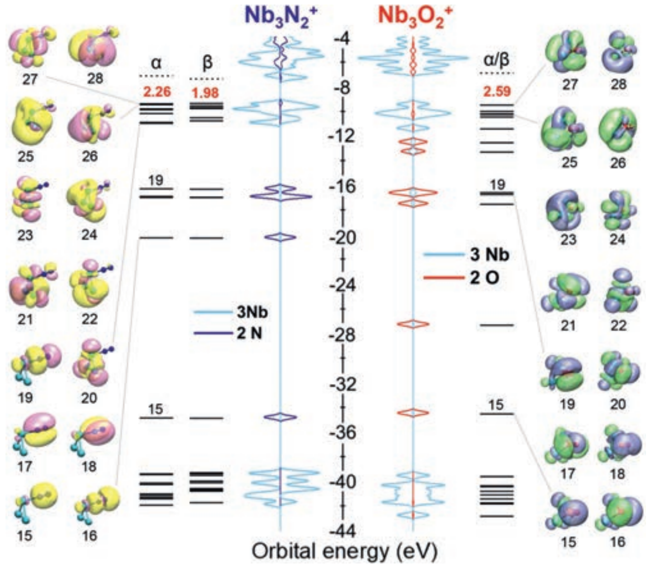

Fig. 3. Energy level of $Nb_3N_2^+$ and $Nb_3O_2^+$ together with PDOS of 2 N atoms and 3 Nb atoms in $Nb_3N_2^+$ and PDOS of 2 O atoms and 3 Nb atoms in $Nb_3O_2^+$. Insets show the corresponding orbitals.

every WBI of O-O bond changes to about 1 from O=O double bond in the ground state oxygen molecule, and the bond length elongated from 1.2 Å to 1.4~1.5 Å), which is similar to O-O bond length and bonding mode in H_2O_2, as named peroxy bond (or peroxide state) after a chemical adsorption. Moreover, every O atom links to 2 Nb atoms in the 3Nb-2O elementary units when $n \geq 3$, showing two types of O–Nb bonds with a minor different WBI, that is, O(1)-Nb(1,2) and O(2)-Nb(1,3) bond. It is notable that $Nb_2O_2^+$ possesses 4 equal Nb-O bonds (WBI = 0.48) and the WBI of O-O bond is 1.02. In all, the WBI of every Nb-N and Nb-O provides detailed information of their bonding strengths.

We have conducted orbital analysis to reveal the essential interaction of Nb_n^+ with N_2 and O_2. Fig. 3 presents a comparison for the partial density of states (PDOS) and corresponding orbitals of 2 N(/O) atoms and linked 3 Nb atoms typically in $Nb_3N_2^+$ and $Nb_3O_2^+$ respectively. Firstly, the overlap area in PDOS of $Nb_3O_2^+$ is much more than $Nb_3N_2^+$. For $Nb_3N_2^+$, this is displayed by the reconstituted $Nb_3N_2^+$ orbital which possesses a pattern involving both the cluster and nitrogen molecule. The PDOS of non-dissociative adsorption of N_2 gives rise to seen as σ_{2s}, σ^*_{2s}, σ_{2pz} which are associated with the dominant $N_2 \rightarrow Nb_3^+$ σ donation interactions, and two equivalent orbitals π_{2px} and π_{2py} involving very few interactions, vacant π^*_{2px} and π^*_{2py} of nitrogen are associated with the $Nb_3^+ \rightarrow N_2$ π backdonation interactions (detailed orbital information including the natural atomic orbital (NAO) contributions is seen in Table S5 in Supporting information) [50]. While in $Nb_3O_2^+$, the interacting orbitals also possess character of free O_2 molecule, where corresponding to σ_{2s}, σ^*_{2s}, σ_{2pz} of oxygen refer to $O_2 \rightarrow Nb_3^+$ σ donation, and two equivalent orbital π_{2px} and π_{2py} both contribute to the $O_2 \rightarrow Nb_3^+$ π donation interaction; meanwhile, the strong DOS correlative to π^*_{2px} and π^*_{2py} of oxygen accounts for the $Nb_3^+ \rightarrow O_2$ dominant π backdonation (Table S5) [51]. Similarly, the NAO analyses for $Nb_6N_2^+$ and $Nb_6O_2^+$ are given in Table S6 (Supporting information).

Further, we conducted energy decomposition analysis based on natural orbitals for chemical valence (EDA-NOCV) [52-55]. The typical results of $Nb_3N_2^+$ and $Nb_3O_2^+$ are shown in Table 3, where the strength of the intrinsic interaction energies (ΔE_{int}) are divided into three components ($\Delta E_{\text{int}} = \Delta E_{\text{pauli}} + \Delta E_{\text{elstat}} + \Delta E_{\text{orb}}$) corresponding to pauli exclusion (ΔE_{pauli}), electrostatic interaction (ΔE_{elstat}) and orbital interaction (ΔE_{orb}) which can be further divided into σ donation, π donation, π backdonation, polarization and the rest interactions. For $Nb_3N_2^+$, ΔE_{elstat} and ΔE_{orb} each contributes a half of the attractive interactions; while in $Nb_3O_2^+$, the ΔE_{orb} contributes about 60%. In total orbital interactions, the $N_2 \rightarrow Nb_3^+$ σ donation interaction and polarization interaction contribute ~48%; $Nb_3^+ \rightarrow N_2$ π backdonation contributes ~40%. In contrast for $Nb_3O_2^+$, ΔE_{orb} is much larger than ΔE_{elstat} in total interactions, among which and the two $O_2 \rightarrow Nb_3^+ \pi$ donation interactions contribute only ~13%, reversely, $Nb_3^+ \rightarrow O_2$ π backdonation contributes ~83% of the interactions. It is worth mentioning that the interacting fragments $^3Nb_3^+$ and $^3O_2$ are both in spin triplet, but $^1Nb_3O_2^+$ in singlet state, which results in a larger value of ΔE_{int} than the BE in forming $Nb_3O_2^+$ because of the differences between the unactivated fragments and the activated complex (which involves an additional energy to activate the precursor).

Fig. 4 displays the principal orbitals correlation diagrams of $Nb_3N_2^+$ and $Nb_3O_2^+$ based on the corresponding fragments, with only α-orbitals being shown as the correlation of β-orbitals is similar. In $Nb_3N_2^+$ (Fig. 4a), $N_2 \rightarrow Nb_3^+$ σ donation interaction dominantly forms compound orbital HOMO-8, which is mainly contributed (about 83%) by HOMO of N_2 (σ_{2pz}) and vacant LUMO+1 orbital of Nb_3^+; and $Nb_3^+ \rightarrow N_2$ π backdonation forms new compound orbitals (HOMO, HOMO-1, HOMO-6) which are composed by the occupied orbitals of Nb_3^+ and LUMO of N_2 ($\pi^*_{2px/y}$). In $Nb_3O_2^+$ as a comparison (Fig. 4b), two $O_2 \rightarrow Nb_3^+$ π donation interactions form HOMO-8, HOMO-9 orbitals of the complex, which are mainly from the occupied antibonding HOMO (π^*_{2px}) and one of the degenerate orbitals (π_{2py}) of O_2, coupled with vacant orbitals (LUMO, LUMO+1) of Nb_3^+. Here π backdonation interactions sourcing from bonding orbitals of Nb_3^+ and LUMO (π^*_{2py}) of O_2 ($Nb_3^+ \rightarrow O_2$) play a dominant contribution and form HOMO-7 orbital of the $Nb_3O_2^+$ complex. The electrons on O_2 fragment π^*_{2py} orbital (Fig. S14 in Supporting information) stem from charge transfer and orbital interactions [56,57]. In addition, NOCV analysis including detailed values of interaction energies and the shapes of electron deformation densities ($\Delta\rho$) are shown in Figs. S17 and S18 (Supporting information), which display the weak interaction/bonding

Table 3
EDA results for $^3Nb_3N_2^+$ and $^1Nb_3O_2^+$ at the B3LYP/TZP level of theory using ADF, taking Nb_3^+ and N_2 (/O_2) as interacting fragments. ΔE_{int} is the intrinsic interaction energies. ΔE_{pauli} is the repulsion energy caused by the Pauli exclusion principle. ΔE_{elstst} and ΔE_{orb} are the attraction energies due to electrostatic and orbital interactions, respectively. The values in parentheses show the contribution to ΔE_{int} and the total orbital interaction ΔE_{orb}.

$^3Nb_3N_2^+$		$^1Nb_3O_2^+$	
Energy term & assignment	kcal/mol	Energy term & assignment	kcal/mol
ΔE_{int}	−13.6	ΔE_{int}	−170.6
ΔE_{pauli}	66.8	ΔE_{pauli}	544.5
ΔE_{ele}	−39.6 (49.2%)	ΔE_{ele}	−287.1 (40.2%)
ΔE_{orb}	−40.9 (50.8%)	ΔE_{orb}	−430.0 (59.8%)
$\Delta E_{orb\text{-}\alpha(1):}$ σ donation + polarization	−10.3 (25.1%)	$\Delta E_{orb\text{-}\alpha(1):}$ π backdonation	−177.8 (41.5%)
$\Delta E_{orb\text{-}\alpha(2):}$ π backdonation	−4.1 (10.1%)	$\Delta E_{orb\text{-}\alpha(2):}$ π donation	−20.0 (4.7%)
$\Delta E_{orb\text{-}\alpha(3):}$ polarization + π backdonation	−3.0 (7.3%)	$\Delta E_{orb\text{-}\alpha(3):}$ π donation	−8.3 (1.9%)
$\Delta E_{orb\text{-}\beta(1)}$: σ donation + polarization	−9.5 (23.3%)	$\Delta E_{orb\text{-}\beta(1):}$ π backdonation	−177.8 (41.5%)
$\Delta E_{orb\text{-}\beta(2):}$ π backdonation	−5.8 (14.2%)	$\Delta E_{orb\text{-}\beta(2):}$ π donation	−20.0 (4.7%)
$\Delta E_{orb\text{-}\beta(3):}$ π backdonation	−3.2 (7.9%)	$\Delta E_{orb\text{-}\beta(3):}$ π donation	−8.3 (1.9%)
$\Delta E_{orb(4):}$ rest	−5.0 (12.2%)	$\Delta E_{orb(4):}$ rest	−16.0 (3.7%)

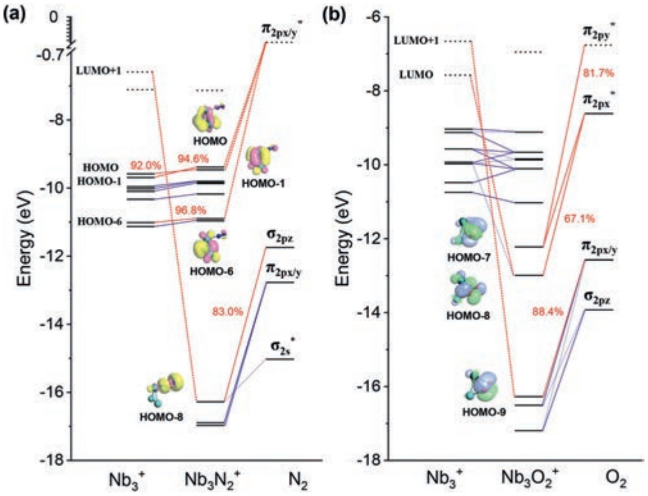

Fig. 4. Kohn–Sham orbital correlation diagrams of (a) $Nb_3N_2^+$in the triplet state. (b) $Nb_3O_2^+$in the stable triplet state. Blue lines are for orbitals composited by one part, and red lines are for orbitals interaction of two fragments with percentage which solid lines are for occupied orbitals and dotted line are for vacant orbitals. All the data are calculated at the B3LYP/TZP level of theory using ADF.

between Nb_3^+ and N_2, while much larger donor-acceptor interaction energies for $Nb_3O_2^+$ in the single state.

Figs. 5a and b present the potential scan curves of Nb_3^+ in reacting with N_2 and O_2 respectively to form the products (more details of varying directions are given in Figs. S20 and S21 in Supporting information), where the NPA charge distribution is displayed in color with dependence on the varying distances of the reactants. For "$Nb_3^+\cdots N_2$" (Fig. 5a), the two overlap curves display minor vibration of the N-N bond distance ranging from 1.09 Å to 1.11 Å. Considering that the product $^1Nb_3O_2^+$has an altered spin multiplicity and oxygen state comparing with the nascent $^3Nb_3^+$ and $^3O_2$, we have performed the potential scan from two directions, allowing the geometrical configuration and spin multiplicity to be equal to the reactants and the products respectively. As is shown in Fig. 5b, the two scanning curves for "$Nb_3^+\cdots O_2$" display a crossing at ~2.4 Å, which indicates a critical value for the interaction distance of chemical reaction, and the energy minima point at a $Nb_3^+\cdots O_2$ distance of 1.74 Å corresponds to the oxygen-activated state (*i.e.*, $^1\Delta_g$ state, with O-O bond distance at 1.44 Å). Furthermore, Kohn–Sham orbital correlation diagrams, charge transfer diagrams along with orbital interactions and detailed NOCV analysis of $Nb_3O_2^+$ in imaginary quintuplet state at a $Nb_3^+\cdots O_2$ distance of 1.80 Å and O-O bond distance of 1.20 Å are shown in Figs. S13, S15 and S19 in Supporting information).

Having unveiled the different interactions involved in "Nb_3^+ + N_2" and "Nb_3^+ + O_2", we then plotted the reaction coordinates for the reaction dynamics of the niobium clusters with oxygen and nitrogen, as shown in Fig. 6. Two reaction pathways are considered for Nb_3^+ with N_2 in view of the likely varying molecular orientation of dinitrogen in approaching the cluster. As is shown, when the dinitrogen takes an end-on adsorption on a vertex atom of the Nb_3^+ cluster (black line), it gets a 0.62 eV energy gain but subsequent path toward the final dissociative $Nb_3N_2^+$ needs to overcome a few endothermic steps and the rate-determine transition state TS3 is 0.27 eV higher than the relative energy of the reactants. Alternatively, if the dinitrogen molecule could approach the cluster via an orientation orthogonal to one of the triangular edges of the Nb_3^+, the reaction path (green line) needs to overcome a relatively smaller energy barrier but the rate-determine TS1 is still 0.24 eV higher in energy than the reactants. This energy barrier is small especially when considering the N≡N bond dissociation energy of ~9.79 eV, but it could not proceed spontaneously in the thermalized flow tube reactors (where previous studies suggest a threshold value could be ~0.1 eV by taking into consideration of vibrational, rotational and translational kinetic energy) [56,58].

In sharp contrast, the reaction of "Nb_3^+ + O_2" is largely exothermic (8.10 eV in our calculation) to form an oxygen-dissociative products with two bridge oxygen atoms bonding to two edges of the triangular Nb_3^+ cluster, and the spin multiplicity turns to be singlet indicative of spin accommodation in the reaction process of $^3Nb_3^+$ with $^3O_2$ [48,59]. Note that, this reaction to form oxygen-dissociated product is highly thermodynamic and also kinetics-favorable, with the TS1 being 2.33 eV (or 3.2 eV for the yellow line) lower than the total energy of the reactants. Therefore, the mass spectrometry observation of $Nb_3O_2^+$ (and the other $Nb_nO_2^+$) could be completely dissociated products. This is largely due to the large Nb-O bond energy (~770 kJ/mol) in contrast to the bond strengths of O-O (~400 kJ/mol) and Nb-Nb (~513 kJ/mol). The large amount of energy release by dissociative adsorption makes it feasible to produce odd-oxygen produts (*e.g.*, $Nb_2O^{+/0}$, $Nb_nO_{1,3}^+$) along with the $NbO^{0/+}$ removal.

In summary, utilizing our customized instrument MIFT-TQMS we report here an in-depth study to compare the gas-phase reactivity of Nb_n^+ clusters with N_2 and O_2. Under sufficient backing gas pressure (up to 1 Torr), the Nb_n^+ clusters readily react with N_2 and form a series of adsorption products Nb_nN_{2m}. In comparison, the Nb_n^+ clusters react with O_2 in a comparable rate but produce $Nb_nO_{1-4}^+$along with a rapidly growing product NbO^+, showing the O-O bond dissociation and metal cluster etching reactions akin to

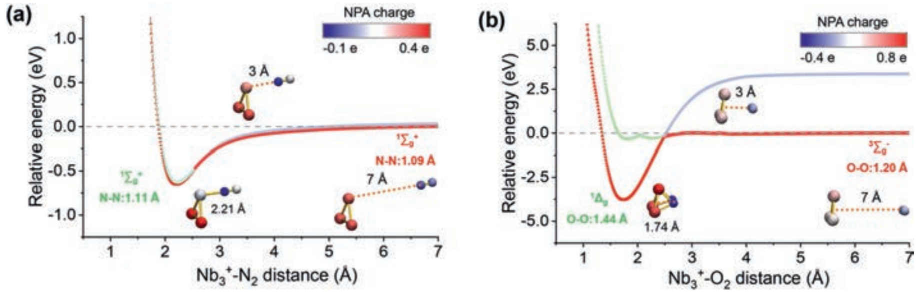

Fig. 5. Potential scan curves of the Nb_3^+ cluster in approaching (a) N_2 and (b) O_2 from two directions with the geometrical configuration and spin multiplicity equal to the reactants and the products respectively. Red lines refer to real approaching process due to energy crossing point, while light blue/green lines refer to imaginary scanning processes. The insets show the NPA charge of every atom as a function of different interaction distance.

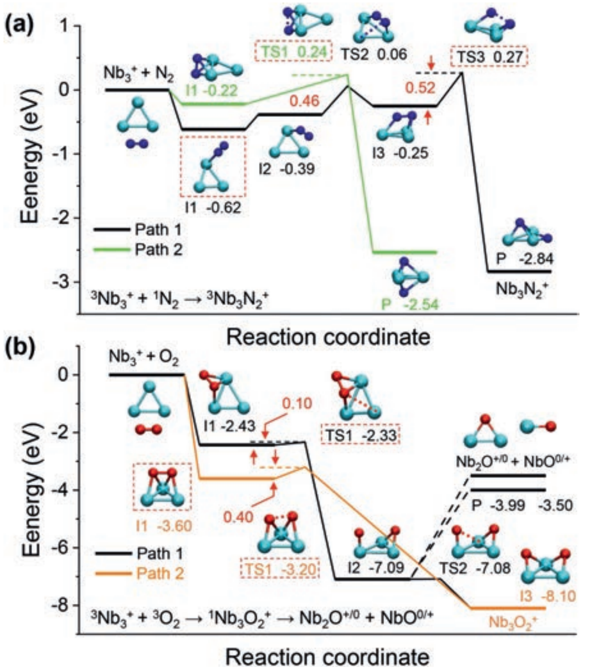

Fig. 6. The calculated reaction pathways for (a) "$Nb_3^+ + N_2$" and (b) "$Nb_3^+ + O_2$". All the thermodynamic data are calculated at the B3LYP/Lanl2dz for Nb and B3LYP/6-311G (d) for O and N.

the previous findings on anionic aluminum and cobalt clusters. Energetics calculations show that the adsorption energies of $Nb_nO_2^+$ (2.5~4 eV) are significantly larger than that of $Nb_nN_2^+$ (0.5~0.9 eV). While the dinitrogen all follow an end-on orientation adsorption on the Nb_n^+ clusters, the chemisorptive $Nb_nO_2^+$ species conform to hollow-site adsorption along with spin-flip and perfect accommodation to be singlet. PDOS and frontier orbital analyses reveal strong π backdonation from Nb_n^+ to O_2; which is in contrast to the $Nb_nN_2^+$ system which involves both σ donation from N_2 to Nb_n^+ and simultaneously weak π backdonation from Nb_n^+ to N_2. Potential scan plots a van der Waals curve for the N_2 molecule in approaching the Nb_3^+ cluster, whereas the potential scan for "$Nb_3^+ \cdots O_2$" displays a crossing from two directions with the spin multiplicity equal to the reactants and the products respectively, shedding light on the spin crossing effect. Further, reaction dynamics calculation unveils feasible O-O bond dissociation and finally NbO (/NbO^+) removal from such $Nb_nO_{2m}^+$ clusters.

Declaration of competing interest

The authors declare that they have no known competing financial interests or personal relationships that could have appeared to influence the work reported in this paper.

Acknowledgments

This work was financially supported by the CAS Instrument Development Project (No. Y5294512C1), the National Natural Science Foundation of China (No. 21722308) and Key Research Program of Frontier Sciences (CAS No. QYZDBSSWSLH024).

Supplementary materials

Supplementary material associated with this article can be found, in the online version, at doi:10.1016/j.cclet.2021.04.020.

References

[1] M. Schmidt, A. Masson, H.P. Cheng, C. Bréchignac, ChemPhysChem 16 (2015) 855–865.
[2] M.B. Knickelbein, Annu. Rev. Phys. Chem. 50 (1999) 79–115.
[3] S.K. Loh, L. Lian, P.B. Armentrout, J. Am. Chem. Soc. 111 (1989) 3167–3176.
[4] M.B. Knickelbein, S. Yang, J. Chem. Phys. 93 (1990) 5760–5767.
[5] W.J.C. Menezes, M.B. Knickelbein, J. Chem. Phys. 98 (1993) 1856–1866.
[6] V. Kumar, Y. Kawazoe, Phys. Rev. B 65 (2002) 125403.
[7] W. Fa, C. Luo, J. Dong, Phys. Rev. B 71 (2005) 245415.
[8] P.V. Nhat, V.T. Ngan, M.T. Nguyen, J. Phys. Chem. C 114 (2010) 13210–13218.
[9] N.P. Vu, N.V. Thi, T.T. Ba, N.M. Tho, J. Phys. Chem. A 115 (2011) 3523–3535.
[10] C. Berkdemir, S.-B. Cheng, A.W. Castleman, Int. J. Mass. Spectrom. 365-366 (2014) 222–224.
[11] C.Q. Jiao, B.S. Freiser, J. Phys. Chem. 99 (1995) 10723–10730.
[12] J.L. Elkind, F.D. Weiss, J.M. Alford, R.T. Laaksonen, R.E. Smalley, J. Chem. Phys. 88 (1988) 5215–5224.
[13] M.E. Geusic, M.D. Morse, R.E. Smalley, J. Chem. Phys. 82 (1985) 590–591.
[14] A.B. Vakhtin, K. Sugawara, Chem. Phys. Lett. 299 (1999) 553–560.
[15] A.B. Vakhtin, K. Sugawara, J. Chem. Phys. 115 (2001) 3629–3639.
[16] S.K. Loh, L. Lian, P.B. Armentrout, J. Chem. Phys. 91 (1989) 6148–6163.
[17] P.P. Radi, G. von Helden, M.T. Hsu, P.R. Kemper, M.T. Bowers, Int. J. Mass. Spectrom. 109 (1991) 49–73.
[18] M.D. Morse, M.E. Geusic, J.R. Heath, R.E. Smalley, J. Chem. Phys. 83 (1985) 2293–2304.
[19] A. Bérces, P.A. Hackett, L. Lian, S.A. Mitchell, D.M. Rayner, J. Chem. Phys. 108 (1998) 5476–5490.
[20] L. Song, A. Eychmueller, R.J. St. Pierre, M.A. El-Sayed, J. Chem. Phys. 93 (1989) 2485–2490.
[21] L. Holmgren, M. Andersson, A. Rosén, Surf. Sci. 331-333 (1995) 231–236.
[22] H. Gronbeck, A. Rosen, Phys. Rev. B 54 (1996) 1549–1552.
[23] Q.F. Wu, S.H. Yang, Int. J. Mass. Spectrom. 184 (1999) 57–65.
[24] D.J. Harding, T.A. Oliver, T.R. Walsh, et al., Eur. J. Mass. Spectrom. 15 (2009) 83–90.
[25] L. Song, M.A. Elsayed, J. Chem. Phys. 94 (1990) 7907–7913.
[26] C. Berg, T. Schindler, G. Niedner-Schatteburg, V.E. Bondybey, J. Chem. Phys. 102 (1995) 4870–4884.
[27] J.M. Parnis, E. Escobar-Cabrera, M.G. Thompson, et al., J. Phys. Chem. A 109 (2005) 7046–7056.
[28] S.R. Miller, T.P. Marcy, E.L. Millam, D.G. Leopold, J. Am. Chem. Soc. 129 (2007) 3482–3483.
[29] B. Pfeffer, S. Jaberg, G. Niedner-Schatteburg, J. Chem. Phys. 131 (2009) 194305.
[30] X. Tang, Y. Hou, C.Y. Ng, B. Ruscic, J. Chem. Phys. 123 (2005) 074330.

[31] M.R. Zakin, R.O. Brickman, J. Chem. Phys. 127 (1988) 3555–3560.
[32] J. Mwakapumba, K.M. Ervin, Int. J. Mass Spectrom. Ion Processes 161 (1997) 161–174.
[33] E.D. Pillai, T.D. Jaeger, M.A. Duncan, J. Am. Chem. Soc. 129 (2007) 2297–2307.
[34] M.A. Addicoat, K.F. Lim, G.F. Metha, J. Chem. Phys. 137 (2012) 034301.
[35] Z. Luo, W.H. Woodward, J.C. Smith, A.W. Castleman Jr., Int. J. Mass. Spectrom. 309 (2012) 176–181.
[36] J.P. Perdew, Phys. Rev. B 34 (1986) 7406.
[37] C. Lee, W. Yang, R.G. Parr, Phys. Rev. B 37 (1988) 785–789.
[38] T. Lu, F. Chen, J. Comput. Chem. 33 (2012) 580–592.
[39] W. Humphrey, A. Dalke, K. Schulten, J. Mol. Graphics Modell. 14 (1996) 33–38.
[40] E.J. Baerends, T. Ziegler, J. Autschbach, et al., ADF2018, SCM, Theoretical Chemistry, Vrije Universiteit, Amsterdam, The Netherlands. http://www.scm.com.
[41] G.G. te Velde, F.M. Bickelhaupt, E.J. Baerends, et al., J. Comput. Chem. 22 (2001) 931–967.
[42] H. Zhang, H. Wu, Y. Jia, et al., Rev. Sci. Instrum. 90 (2019) 073101.
[43] K.A. Zemski, D.R. Justes, A.W. Castleman, J. Phys. Chem. B 106 (2002) 6136–6148.
[44] J.R. Sambrano, L. Gracia, J. Andrés, S. Berski, A. Beltrán, J. Phys. Chem. A 108 (2004) 10850–10860.
[45] J.E. Bower, J. Chem. Phys. 85 (1986) 5373–5375.
[46] R.E. Leuchtner, A.C. Harms, A.W. Castleman Jr., J. Chem. Phys. 91 (1989) 2753–2754.
[47] E. Kapiloff, K.M. Ervin, J. Phys. Chem. A 101 (1997) 8460–8469.
[48] Z. Luo, G.U. Gamboa, J.C. Smith, et al., J. Am. Chem. Soc. 134 (2012) 18973–18978.
[49] R. Burgert, H. Schnöckel, A. Grubisic, X. Li, S.T. Stokes, Science 319 (2008) 438–442.
[50] C. Geng, J. Li, T. Weiske, H. Schwarz, Proc. Natl. Acad. Sci. U. S. A. 115 (2018) 11680–11687.
[51] N. Chen, R.T. Yang, Ind. Eng. Chem. Res. 35 (1996) 4020–4027.
[52] M.P. Mitoraj, A. Michalak, T. Ziegler, J. Chem. Theory. Comput. 5 (2009) 962–975.
[53] T. Ziegler, A. Rauk, Theor. Chim. Acta 46 (1977) 1–10.
[54] F.M. Bickelhaupt, E.J. Baerends, Rev. Comput. Chem. 15 (2000) 1–86.
[55] M.V. Hopffgarten, G. Frenking, Wiley Interdiscip. Rev. Comput. Mol. Sci. 2 (2012) 43–62.
[56] J. Chen, H. Zhang, X. Liu, et al., Phys. Chem. Chem. Phys. 18 (2016) 7190–7196.
[57] J. Chen, Z. Luo, J. Yao, Phys. Chem. Chem. Phys. 19 (2017) 21777–21782.
[58] Z. Luo, S. Khanna, Springer Nature Singapore Pte Ltd., Springer, 2020, p. 267.
[59] A.C. Reber, S.N. Khanna, P.J. Roach, W.H. Woodward, A.W. Castleman, J. Am. Chem. Soc. 129 (2007) 16098–16101.